A&A 518, L82 (2010)
DOI: 10.1051/0004-6361/201014625

Astronomy & Astrophysics
Special feature

Herschel: the first science highlights

Letter to the Editor

Herschel⋆-SPIRE spectroscopy of G29.96-0.02: Fitting the full SED

J. M. Kirk[1], E. Polehampton[2,3], L. D. Anderson[4], J.-P. Baluteau[4], S. Bontemps[5], C. Joblin[9,10], S. C. Jones[3], D. A. Naylor[3], D. Ward-Thompson[1], G. J. White[2,17], A. Abergel[6], P. Ade[1], P. André[7], H. Arab[6], J.-P. Bernard[9,10], K. Blagrave[15], F. Boulanger[6], M. Cohen[11], M. Compiegne[15], P. Cox[12], E. Dartois[6], G. Davis[13], R. Emery[2], T. Fulton[19], C. Gry[4], E. Habart[6], M. Huang[14], G. Lagache[6], T. Lim[2], S. Madden[7], G. Makiwa[3], P. Martin[15], M.-A. Miville-Deschênes[6], S. Molinari[16], H. Moseley[18], F. Motte[7], K. Okumura[7], D. Pinheiro Gonçalves[15], J. A. Rodón[4], D. Russeil[4], P. Saraceno[16], S. Sidher[2], L. Spencer[3], B. Swinyard[2], and A. Zavagno[4]

(Affiliations are available in the online edition)

Received 31 March 2010 / Accepted 10 May 2010

ABSTRACT

We use the SPIRE Fourier-transform spectrometer (FTS) on-board the ESA *Herschel* Space Observatory to analyse the submillimetre spectrum of the Ultra-compact HII region G29.96-0.02. Spectral lines from species including ^{13}CO, CO, [CI], and [NII] are detected. A sparse map of the [NII] emission shows at least one other HII region neighbouring the clump containing the UCHII. The FTS spectra are combined with ISO SWS and LWS spectra and fluxes from the literature to present a detailed spectrum of the source spanning three orders of magnitude in wavelength. The quality of the spectrum longwards of 100 μm allows us to fit a single temperature greybody with temperature 80.3 ± 0.6 K and dust emissivity index 1.73 ± 0.02, an accuracy rarely obtained with previous instruments. We estimate a mass of 1500 $M_\odot$ for the clump containing the HII region. The clump's bolometeric luminosity of 4×10^6 $L_\odot$ is comparable to, or slightly greater than, the known O-star powering the UCHII region.

Key words. HII regions – stars: formation – submillimetre: ISM – ISM: individual objects: G29.96-0.02

1. Introduction

Ultra-compact HII (UCHII) regions are small nebulae that surround massive, young stars that are still embedded within a natal cloud (Churchwell 2002; Hoare et al. 2007). UCHII regions represent an important evolutionary stage in the formation of massive stars. They may correspond to the still embedded accretion phase while the star is already ionising its surroundings. Their study is critical to our understanding of how stars manage to reach high masses despite the high pressure generated by their growing HII regions. UCHII regions are amongst the brightest Galactic objects at submillimetre wavelengths and can be used as a probe of star formation in distant galaxies. Thus, they make excellent candidates with which to probe all phases of massive star formation and with which to test new instruments.

G29.96-0.02 is an UCHII region (Wood & Churchwell 1989; Peeters et al. 2002) located at a distance of $8.9^{+0.6}_{-0.09}$ kpc (Sewilo et al. 2004). The bright IR source at the centre of G29.96-0.02 is an O5-6 star (Watson & Hanson 1997; Martín-Hernández et al. 2003), with a luminosity of $L_{\rm bol} \sim 3{-}4 \times 10^6$ $L_\odot$ for the Watson & Hanson (1997) temperature limits at the Sewilo et al. (2004) distance. However, models indicate that a cluster of young stars must be present in G29.96-0.02 to account for its observed luminosity (Lumsden et al. 2003).

At the head of the cometary shaped radio emission (Wood & Churchwell 1989) is a small cluster of hot molecular cores (~300 K) with masses of 3–11 $M_\odot$ (Beuther et al. 2007). These arcsec-sized structures are embedded within an arcmin-sized submillimetre clump called G29.956-0.017SMM (Thompson et al. 2006). Fey et al. (1995) suggested that the cometary shape of the UCHII region is caused by its expansion westwards into the denser part of the surrounding clump. This clump is part of a larger complex that has been mapped by *Herschel*-SPIRE/PACS as part of the Hi-GAL key programme (Molinari et al. 2010; Beltran et al. in prep.).

In this paper we present new submillimetre spectra taken towards G29.956-0.017SMM (hereafter G29) with the ESA *Herschel* Space Observatory (Pilbratt et al. 2010) as part of the "Evolution of Interstellar Dust" key programme (Abergel et al. 2010). The data were taken with the SPIRE Fourier-transform spectrometer (FTS). The SPIRE instrument, its in-orbit performance, and its scientific capabilities are described by Griffin et al. (2010), and the SPIRE astronomical calibration methods and accuracy are outlined by Swinyard et al. (2010).

2. Observations

G29 was observed with the high-resolution mode of the SPIRE FTS on 13 September, 2009 at 19:49 (*Herschel* observation ID, 1342183824). Two scan repetitions were observed giving an on-source integration time of 266.4 s. The pointing centre was at a right ascension and declination (J2000) of $18^{\rm h}46^{\rm m}04.07^{\rm s}$, $-02°39'21''.88$ and Galactic coordinates of 29.9561, −0.01726. The unapodized spectral resolution was 1.2 GHz (0.04 cm^{-1}), after apodization (using extended Norton-Beer function 1.5, Naylor & Tahic 2007) this became 2.17 GHz.

The SPIRE FTS measures the Fourier-transform of the source spectrum across short (SSW, 194–313 μm) and long

⋆ *Herschel* is an ESA space observatory with science instruments provided by European-led Principal Investigator consortia and with important participation from NASA.

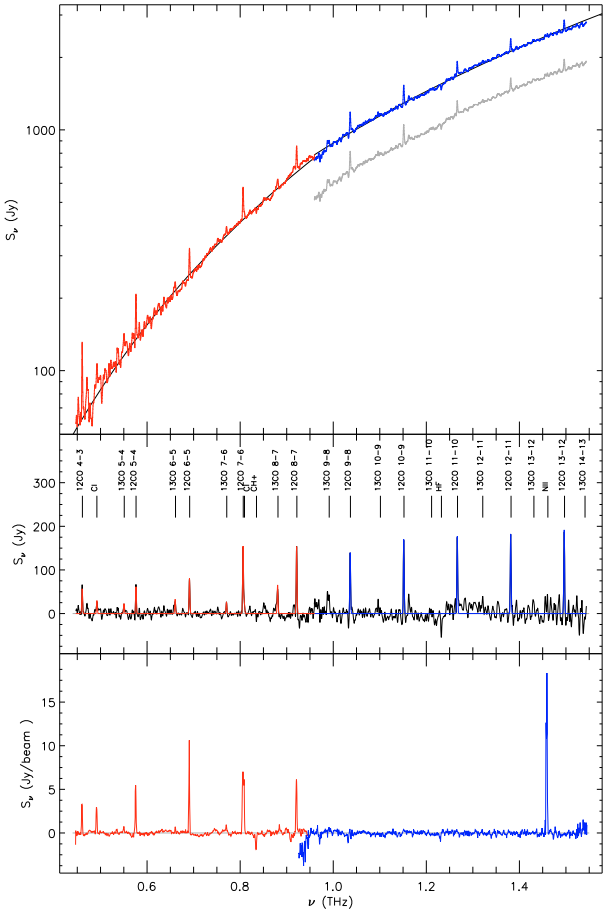

Fig. 1. SPIRE FTS SLWC3 (red) and SSWD4 (blue/grey) spectra of G29. *Upper*: On-source spectrum with continuum, point-source calibration. *Middle*: As above with continuum subtracted. Major lines are annotated. *Lower*: Mean off-source spectrum, extended calibration. See text for details.

(SLW, 303–671 μm) wavelength bands simultaneously. Each waveband is imaged with a hexagonal bolometer array with pixel spacing of approximately twice the beam-width. The *FWHM* beam-widths of the SSW and SLW arrays vary between 17–21″ and 29–42″ respectively. The source spectrum, including the continuum, is restored by taking the inverse transform of the observed interferogram. For details of the SPIRE FTS and its calibration see Griffin et al. (2010) and Swinyard et al. (2010).

3. Results

The upper panel of Fig. 1 shows the apodized SLW (red) and SSW (grey) spectra. Only the data from the central bolometer (C3 for the SLW and D4 for the SSW) as calibrated for a point source are shown for each spectrum. The spectra are dominated by the thermal continuum. Superimposed on this are a series of bright lines, the most noticeable of which are the ladder of CO lines. The shape of the continuum was estimated by masking the CO lines and performing a linear regression of the form $\log S_\nu = C + p \log \nu$ to both spectra. The data were best fit by power-laws with indices of $p_{\rm SSW} = 2.71$ and $p_{\rm SLW} = 3.40$ respectively. There is a disconnect between the two spectra. The offset in power-law constants was $C_{\rm SSW} - C_{\rm SLW} = 0.164$, equivalent to a linear factor of 1.45. The SSW spectrum was shifted upwards by this margin and replotted as the blue spectrum under the assumption that the discontinuity was due to differing structure within the SLW and SSW beams. The power-laws for each spectrum are plotted as black lines.

Table 1. Best fit line parameters.

Species	Line	Band	ν [GHz]	$\nu_{\rm offset}$ [GHz]	$S_{\rm peak}$ [Jy]
12CO	4–3	SLW	461.0	0.48	57.1 ± 12.6
	5–4	SLW	576.3	0.09	61.6 ± 5.8
	6–5	SLW	691.5	0.36	80.7 ± 1.1
	7–6	SLW	806.7	0.46	154 ± 2
	8–7	SLW	921.8	0.45	154 ± 4
	9–8	SSW	1037.	0.51	140 ± 6
	10–9	SSW	1152.	0.46	170 ± 7
	11–10	SSW	1267.	0.53	179 ± 15
	12–11	SSW	1382.	0.70	183 ± 7
	13–12	SSW	1497.	0.71	192 ± 14
13CO	5–4	SLW	550.9	0.52	22.8 ± 3.4
	6–5	SLW	661.1	0.74	32.9 ± 3.0
	7–6	SLW	771.2	0.61	25.9 ± 4.6
	8–7	SLW	881.3	0.82	65.7 ± 3.8
[C I]		SLW	492.2	-0.08	29.9 ± 6.5
[C I]		SLW	809.3	0.50	26.8 ± 3.3

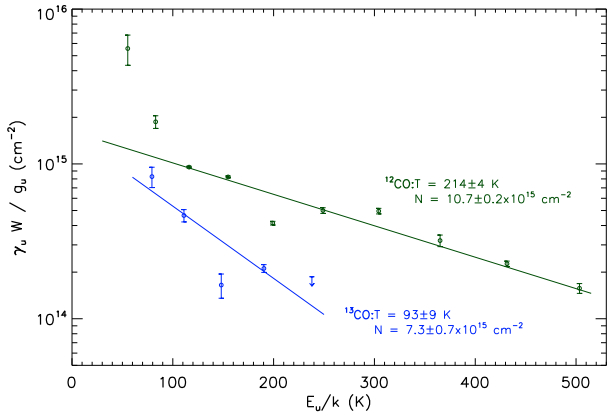

Fig. 2. Population diagram for ^{12}CO and ^{13}CO towards G29.

The Levenberg-Marquardt least-squares minimisation package MPFIT (Markwardt 2009) was used to simultaneously fit a catalogue of lines and an 8th-order polynomial to each of the SLW and SSW spectra. It was assumed that the lines were Gaussian and that the linewidths were not resolved. The middle panel of Fig. 1 shows the spectra after the polynomial background has been subtracted. The best-fit line shapes are shown in red and blue for the SLW and SSW bands respectively. These show the same ladder of CO lines as the upper panel as well as their ^{13}CO counterparts. The position of the ^{12}CO and ^{13}CO lines are annotated (Pickett et al. 1998). The brightest non-CO lines are the 492 and 809 GHz lines of [C I]. The 809 GHz [C I] line is blended with the 806 GHz $J = 7$–6 line of ^{12}CO. Table 1 lists the transitions, reference frequencies, frequency offsets, and peak flux densities for each significant line fit.

Figure 2 shows the rotational population diagram for ^{12}CO in green and ^{13}CO in blue. Following Goldsmith & Langer (1999) we fit a rotational temperature to each species. The weighted linear fits and results are plotted for each species. The quoted errors are the errors on the fit and do not include uncertainties in beam size, calibration, and sub-structure within the beam. The ^{13}CO lines come from a greater depth of material than the ^{12}CO lines and will be more indicative of the temperature of the interior of the clump. The 7–6 transition of ^{13}CO and the 9–8 transition of ^{12}CO appear to be lower than the trends. This could be due to the structure in the beam changing between transitions (the beam *FWHM* changes by a factor of 2.5 between the CO 4–3 and 13–12 transitions).

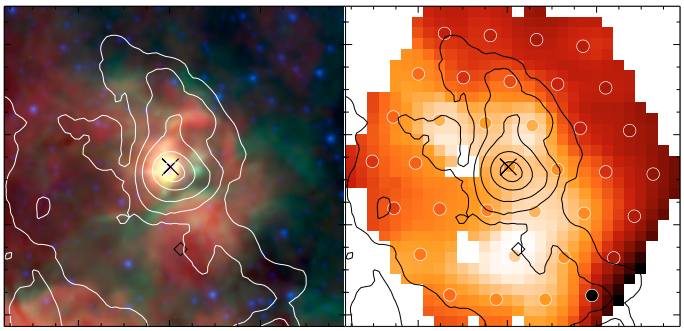

Fig. 3. *Left*: False-colour map of G29 showing GLIMPSE 4.5 (blue) and 8-μm (green) (Benjamin et al. 2003) and MAGPIS 20 cm (red) (Helfand et al. 2006). *Right*: [N II] line flux towards G29. The circles show the position of the bolometers on the sky. The space between them has been interpolated using inverse distance weighting. The X marks the position of the G29.96-0.02 radio source (Wood & Churchwell 1989, $18^h46^m03.96^s$, $-02°39'21''.5$). The diamond marks the position of the NII peak. The contours are SCUBA 850 μm emission (5, 10, 20, 50 and 100 times the local off-source rms) showing the extent of the G29.956-0.017SMM clump.

The region around G29 is shown in the left panel of Fig. 3 as a false-colour image – blue and green are GLIMPSE 4.5 and 8-μm (Benjamin et al. 2003) and red is MAGPIS 20 cm (Helfand et al. 2006) – and archival SCUBA 850 μm contours. The X marks the position of the VLA radio emission associated with the UCHII region (Wood & Churchwell 1989). The spectra measured towards positions surrounding G29 show several notable differences to the on-source spectra. The lower panel of Fig. 1 shows the mean background-subtracted spectrum for co-aligned off-source bolometers. The 835 GHz line of CH^+ is seen in absorption in the SLW band and appears to be probing the ISM (see Naylor et al. 2010, for a detailed decomposition of the CH^+ line for this source). The deepest absorption feature is coincident with the 1.232 THz line of HF (Neufeld et al. 2010). The higher-order ^{12}CO and ^{13}CO lines are not detected in the SSW band, but the 1.46 THz fine structure line of [N II] is strongly detected. This line is present in the extended-source calibration, but not in the on-source point-source calibration.

A fit to the [N II] line was performed for all bolometers of the SLW array. The results are plotted on the right panel of Fig. 3. The coloured circle markers show the bolometer positions and the measured line intensities at those positions. For these early results the bolometer array was not offset to create a fully sampled map. To compensate for this the pixels between the bolometers have been interpolated using an inverse distance weighting (modified Shepard's) method. The southern [N II] peak is coincident with a region of 20 cm emission that is bounded to the north by a 8-μm filament suggesting that it is a separate HII region to the G29 UCHII region. Its diameter is $\sim 1'$ (2.5 pc at 8.9 kpc). The morphology around G29 is clearly complex and a more detailed, fully-sampled study will be required to disentangle the various components. As stated, this preliminary map was not fully sampled, but it does shows the potential of the FTS as a mapping spectrometer.

4. Spectral energy distribution

Figure 4 shows the spectral energy distribution (SED) measured towards G29. SPIRE FTS SLW-C3 and SSW-D4 spectra are shown in the same colours (red and blue) as Fig. 1. A search was made for archival data coincident with G29. For consistency with the FTS data the downloaded spectra and data points were converted into intensity units by dividing by their wavelength-dependent beam area or, where relevant, their aperture area. The archival data is plotted in Fig. 4 and described in the figure caption.

Figure 4 does not include the relative correction applied in Fig. 1. It was found that the FTS SLW data were marginally higher that the SCUBA 450 μm data point and that the first point of the FTS SSW spectrum was significantly higher than the ISO longwave spectrograph (LWS) final data point. It was assumed that the three sections of the long wavelength SED (ISO LWS, FTS SSW, FTS SLW) followed the same single temperature greybody and that the offsets between them were due to differences in their absolute calibration. A greybody equation was fitted to these three spectra and offsets between them accounted for by giving the flux from each section a multiplier coefficient. The greybody had the form

$$I_\nu = C_X B_\nu(T)\left(1 - e^{-(\nu/\nu_c)^\beta}\right) \quad (1)$$

where C_X is the coefficient, $B_\nu(T)$ is the Planck function at temperature T, ν_c is the frequency where the emission becomes optically thin, and β is the dust emissivity index. The data were resampled into evenly spaced bins in log-wavelength space to prevent the differing density of data points between the ISO LWS and the SPIRE FTS corrupting the minimisation.

The best-fit to the SED was $T = 80.3 \pm 0.6$ K, $\beta = 1.73 \pm 0.02$, and $\nu_c = 20.0 \pm 0.5$ THz (equivalent to $\lambda = 15.0 \pm 0.4\,\mu$m). We note that the SED temperature is similar to the ^{13}CO rotational temperature from Fig. 2. The multiplicative coefficients for the FTS SSW and FTS SLW were found to be 9.3 ± 0.08 and 4.04 ± 0.06 respectively, the ISO LWS coefficient was fixed at 1.0. The SPIRE FTS spectra have been aligned to the ISO LWS calibration. A single temperature greybody well fits the data longwards of $\sim$40 μm. However, fitting a single component greybody to a complicated source like G29 can only yield a broadly characteristic temperature. The relatively flat SED shortwards of the peak shows that there must be several hotter temperature components. Nevertheless, Fig. 4 does show that the long wavelength the slope of the SPIRE FTS data is consistent with the slope of the literature data.

In the following paragraphs we adopt the distance of 8.9 kpc (Sewilo et al. 2004) for G29 and assume that the majority of the emission comes from a region comparable to, or smaller than, the Hershel beam at 250 μm ($\theta = 18''$)–(at 850 μm, 60% of the extended emission towards G29 is within the central SCUBA 14.7″ beam, (Thompson et al. 2006)). Based on the fitted dust temperature, G29's published 850 μm peak flux density (Thompson et al. 2006), and making typical assumptions (e.g. Kirk et al. 2005) we estimate the mass of the G29 clump to be $M \sim 1500\ M_\odot$. As with the fitted temperature, the actual mass will depend on the internal profile/geometry of the clump, but we note that this mass is similar to the median mass (940 $M_\odot$) of the infra-red dark clouds (IRDCs) from which high-mass stars are believed to form (Rathborne et al. 2006).

The luminosity integrated under the fitted greybody in the range 2–2000 μm is $L_{\rm Dust} = 61 D^2\theta^2\ L_\odot$ where D is the distance to the source in kpc and θ is the diameter of the emitting area. The above assumptions give a luminosity of $L_{\rm Dust} = 1.6\times10^6\ L_\odot$. This agrees with the luminosity of $10^6\ L_\odot$ estimated from IRAS measurements alone (Wood & Churchwell 1991). Likewise, the bolometric luminosity in the range 2–2000 μm, interpolating to the fitted SED at $\lambda > 650$ μm, is $L_{\rm bol} = 154 D^2\theta^2\ L_\odot$. The greybody luminosity is $\sim$40% of $L_{\rm bol}$. At the assumed distance $L_{\rm bol} = 4.0\times10^6\ L_\odot$. The $L_{\rm bol}$ of the clump containing the UCHII should equal the luminosity of the driving sources if the region is in equilibrium. Our calculated $L_{\rm bol}$ is on the upper limit of

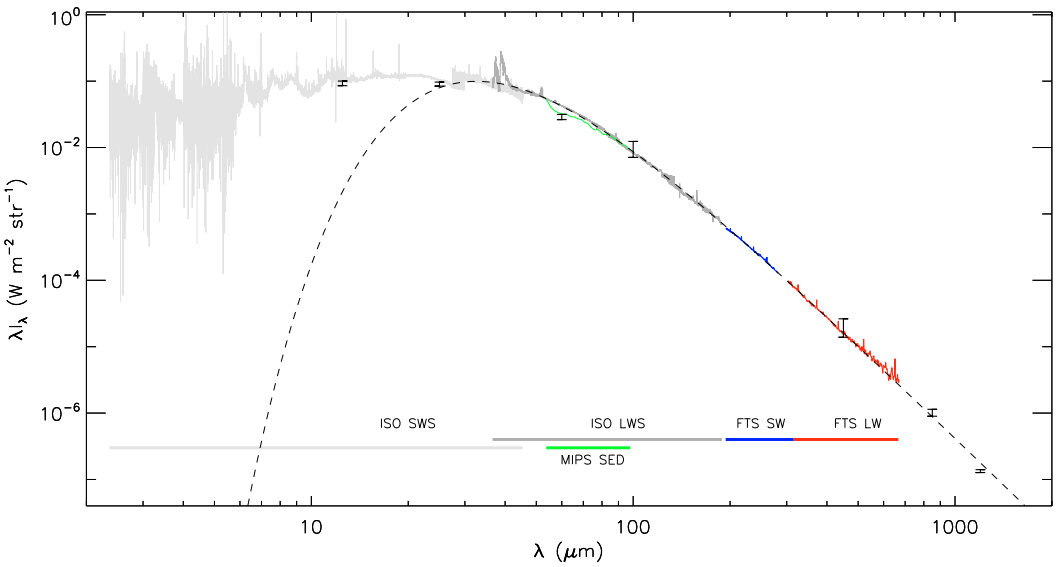

Fig. 4. The G29 spectral energy distribution. SPIRE SWS-D4/SLW-C3 spectra are shown by the blue/red lines. The light and dark grey spectra are archival data from the ISO Short Wavelength Spectrograph (de Graauw et al. 1996, SWS) and ISO Long Wavelength Spectrograph (Clegg et al. 1996, LWS) respectively and were originally published by Peeters et al. (2002). Archival MIPS SED mode data (Rieke et al. 2004) are shown by the green line. The error bars show IRAS 12.5–100 μm (Helou & Walker 1988, IRAS 18434-0242 is coincident with G29), SCUBA 450 and 850 μm (Thompson et al. 2006), and IRTF 1.3 mm (Chini et al. 1986) data points. The FTS SED data have been shifted to the same calibration as the ISO LWS data. A best fit SED is shown by the dashed line.

the range of luminosities for the identified single O-star in G29 ($3-4\times10^6\,L_\odot$, Watson & Hanson 1997) which may support the idea that the luminosity from more than one star is powering the reprocessed SED (Lumsden et al. 2003).

5. Conclusions

We have presented new SPIRE FTS 190–670 μm spectra of the submillimetre clump G29.956-0.017SMM which contains the G29.96-0.02 UCHII region. The impressive capabilities of the SPIRE FTS have allowed us to simultaneously observe both the dust continuum and prominent spectral lines towards G29. We have conducted basic line-fitting and shown the distribution of [N II] emission towards G29. While this preliminary map was not fully sampled it does show at least one other HII region neighbouring G29 and demonstrates the amazing potential of the FTS as a mapping spectrometer. We have reconstructed the SED of G29 using the FTS spectra and archival measurements and have shown that the FTS calibration is broadly consistent with earlier observations. The combined data-set allowed us to fit a precise greybody with $T = 80$ K and $\beta = 1.73$. Based on a distance of 8.9 kpc we estimated the mass of G29 to be approximately 1500 $M_\odot$. The calculated luminosity of the G29 clump is slightly greater than the known O-star at the centre of the UCHII region.

Acknowledgements. We thank D. Neufeld for identifying the 1.2 THz HF absorption feature. J.M.K. acknowledges STFC funding, while this work was carried out, under the auspices of the Cardiff Astronomy Rolling Grant. SPIRE has been developed by a consortium of institutes led by Cardiff University (UK) and including Univ. Lethbridge (Canada); NAOC (China); CEA, LAM (France); IFSI, Univ. Padua (Italy); IAC (Spain); Stockholm Observatory (Sweden); Imperial College London, RAL, UCL-MSSL, UKATC, Univ. Sussex (UK); and Caltech, JPL, NHSC, Univ. Colorado (USA). This development has been supported by national funding agencies: CSA (Canada); NAOC (China); CEA, CNES, CNRS (France); ASI (Italy); MCINN (Spain); Stockholm Observatory (Sweden); STFC (UK); and NASA (USA).

References

Abergel, A., et al. 2010, A&A, 518, L96
Benjamin, R. A., Churchwell, E., Babler, B. L., et al. 2003, PASP, 115, 953
Beuther, H., Zhang, Q., Bergin, E. A., et al. 2007, A&A, 468, 1045
Chini, R., Kreysa, E., Mezger, P. G., & Gemuend, H. 1986, A&A, 154, L8
Churchwell, E. 2002, ARA&A, 40, 27
Clegg, P. E., Ade, P. A. R., Armand, C., et al. 1996, A&A, 315, L38
de Graauw, T., Haser, L. N., Beintema, D. A., et al. 1996, A&A, 315, L49
Fey, A. L., Gaume, R. A., Claussen, M. J., & Vrba, F. J. 1995, ApJ, 453, 308
Goldsmith, P. F., & Langer, W. D. 1999, ApJ, 517, 209
Griffin, M. J., et al. 2010, A&A, 518, L3
Helfand, D. J., Becker, R. H., White, R. L., Fallon, A., & Tuttle, S. 2006, AJ, 131, 2525
Helou, G., & Walker, D. W. 1988, Infrared astronomical satellite (IRAS) catalogs and atlases. The small scale structure catalog, 7
Hoare, M. G., Kurtz, S. E., Lizano, S., Keto, E., & Hofner, P. 2007, Protostars and Planets V, 181
Kirk, J. M., Ward-Thompson, D., & André, P. 2005, MNRAS, 360, 1506
Lumsden, S. L., Puxley, P. J., Hoare, M. G., Moore, T. J. T., & Ridge, N. A. 2003, MNRAS, 340, 799
Markwardt, C. B. 2009, in Astronomical Society of the Pacific Conference Series, ed. D. A. Bohlender, D. Durand, & P. Dowler, ASP Conf. Ser., 11, 251
Martín-Hernández, N. L., Bik, A., Kaper, L., Tielens, A. G. G. M., & Hanson, M. M. 2003, A&A, 405, 175
Molinari, S., et al. 2010, A&A, 518, L100
Naylor, D. A., & Tahic, M. K. 2007, J. Opt. Soc. Am. A, 24, 3644
Naylor, D. A., et al. 2010, A&A, 518, L117
Neufeld, D. A., et al. 2010, A&A, 518, L108
Peeters, E., Martín-Hernández, N. L., Damour, F., et al. 2002, A&A, 381, 571
Pickett, H. M., Poynter, I. R. L., Cohen, E. A., et al. 1998, Journal of Quantitative Spectroscopy and Radiative Transfer, 60, 883
Pilbratt, G. L., et al. 2010, A&A, 518, L1
Rathborne, J. M., Jackson, J. M., & Simon, R. 2006, ApJ, 641, 389
Rieke, G. H., Young, E. T., Engelbracht, C. W., et al. 2004, ApJS, 154, 25
Sewilo, M., Watson, C., Araya, E., et al. 2004, ApJS, 154, 553
Swinyard, B. M., et al. 2010, A&A, 518, L4
Thompson, M. A., Hatchell, J., Walsh, A. J., MacDonald, G. H., & Millar, T. J. 2006, A&A, 453, 1003
Watson, A. M., & Hanson, M. M. 1997, ApJ, 490, L165
Wood, D. O. S., & Churchwell, E. 1989, ApJS, 69, 831
Wood, D. O. S., & Churchwell, E. 1991, ApJ, 372, 199

Page 5 is available in the electronic edition of the journal at http://www.aanda.org

[1] School of Physics and Astronomy, Cardiff University, Queens Buildings, The Parade, Cardiff, CF24 3AA, UK
e-mail: jason.kirk@astro.cf.ac.uk
[2] Space Science & Technology Department, Rutherford Appleton Laboratory, Chilton, Didcot, Oxfordshire OX11 0QX, UK
[3] Institute for Space Imaging Science, University of Lethbridge, 4401 University Dr., Lethbridge, AB, Canada
[4] Laboratoire d'Astrophysique de Marseille, UMR 6110 CNRS, 38 rue F. Joliot-Curie, 13388 Marseille, France
[5] CNRS/INSU, Laboratoire d'Astrophysique de Bordeaux, UMR 5804, BP 89, 33271 Floirac Cedex, France
[6] Institut d'Astrophysique Spatiale, UMR 8617, CNRS/Université Paris-Sud 11, 91405 Orsay, France
[7] CEA, Laboratoire AIM, Irfu/SAp, Orme des Merisiers, 91191 Gif-sur-Yvette, France
[8] IPAC, California Institute for Technology, Pasadena, USA
[9] Université de Toulouse, UPS, CESR, 9 avenue du colonel Roche, 31028 Toulouse Cedex 4, France
[10] CNRS, UMR 5187, 31028 Toulouse, France
[11] University of California, Radio Astronomy Laboratory, Berkeley, 601 Campbell Hall, US Berkeley CA 94720-3411, USA
[12] Institut de Radioastronomie Millimétrique (IRAM), 300 rue de la Piscine, 38406 Saint-Martin-d'Hères, France
[13] Joint Astronomy Centre, University Park, Hilo
[14] National Astronomical Observatories, PR China
[15] Canadian Institute for Theoretical Astrophysics, Toronto, Ontario, M5S 3H8, Canada
[16] Istituto di Fisica dello Spazio Interplanetario, INAF, via del Fosso del Cavaliere 100, 00133 Roma, Italy
[17] Department of Physics & Astronomy, The Open University, Milton Keynes MK7 6AA, UK
[18] NASA – Goddard SFC, USA
[19] Blue Sky Spectroscopy Inc, Lethbridge, Canada